Biosensors and Bioelectronics 142 (2019) 111540

Contents lists available at ScienceDirect

Biosensors and Bioelectronics

journal homepage: www.elsevier.com/locate/bios

Ionic liquid and spatially confined gold nanoparticles enhanced photoelectrochemical response of zinc-metal organic frameworks and immunosensing squamous cell carcinoma antigen

Qiuxi Wei[a], Chen Wang[a], Xue Zhou[a], Tsunghsueh Wu[c], Yanying Wang[a,**], Chunya Li[a,*], Nianjun Yang[b,***]

[a] Key Laboratory of Analytical Chemistry of the State Ethnic Affairs Commission, College of Chemistry and Materials Science, South-Central University for Nationalities, Wuhan, 430074, China
[b] Institute of Materials Engineering, University of Siegen, Siegen, 57076, Germany
[c] Department of Chemistry, University of Wisconsin-Platteville, 1 University Plaza, Platteville, WI, 53818-3099, United States

ARTICLE INFO

Keywords:
Photoelectrochemical immunosensor
Metal-organic frameworks
Ionic liquid
Squamous cell carcinoma antigen
Signal-off sensor

ABSTRACT

Metal-organic framework nanocrystal (Zn-MOF) was synthesized by using 3,3'-{(propane-1,3-diyl)bis[1-(4-carboxybenzyl)-1H-imidazol-3-ium]} hexafluorophosphate ionic liquid as the functional monomer and Zn^{2+} as the central metal ion under hydrothermal conditions. Spatially confined gold nanoparticles (Au-NP) were prepared by *in-situ* reduction of chloroauric acid in the nanopores of Zn-MOF using acetic acid as the reducing agent to fabricate Au-NP@Zn-MOF nanocomposites. Au-NPs@Zn-MOF was further functionalized with 1H-imidazolium-1,3-bis(2-aminoethyl)bromide ionic liquid (IBABr) to prepare IBABr-Au@Zn-MOF nanocomposites. All above-mentioned nanomaterials were thoroughly characterized by TEM, SEM, XPS, FTIR, and nitrogen-adsorption surface area analysis. IBABr-Au@Zn-MOFnanocomposites were then deposited onto a glassy carbon electrode and used as the photoactive element to fabricate a label-free photoelectrochemical (PEC) immunosensor by immobilizing anti-squamous cell carcinoma antigen (anti-SCCA). The PEC sensing principle is based on the photocurrent decline due to the blocking effect of SCCA on the electron and mass transfer after binding SCCA to anti-SCCA. The photocurrent variation related to the specific recognition of SCCA shows a linear relationship to the logarithm of SCCA concentration in the range of 5.0 pg mL^{-1} to 15.0 ng mL^{-1}. The detection limit is as low as 2.34 pg mL^{-1}. Such a signal-off PEC immunosensor is highly selective, sensitive, stable, and reproducible towards SCCA detection. Its performance is comparable to enzyme-linked immunosorbent assay from the studies on clinical samples. This immunosensor is promising for the label-free determining SCCA in clinical human serum samples.

1. Introduction

Since squamous cell carcinoma antigen (SCCA) has been identified as an effective tumor marker for the diagnosis of cervical cancer, it has played a crucial role in the evaluation of tumorigenesis and developing, the therapeutic effect, also in monitoring the prognosis and the recurrence of tumor (Charakora et al., 2018; Kato and Torigoe, 1977). SCCA is often associated with cancer of epithelial or endodermal origin (including lung cancer, melanoma, and hepatocellular carcinoma), making it a potentially versatile diagnostic tool (Sturgeon et al., 2010; Wu et al., 2017; Zhao et al., 2014, 2015). The SCCA concentration in the serum of a healthy adult is less than 1.5 ng mL^{-1}, making the task of determinign SCCA selectively and accurately a huge challenge (Wu et al., 2017). Up to now, the SCCA determination is commonly performed by using enzyme-linked immunosorbent assay, radioimmunoassay, chemiluminescent immunoassay and immunosensor (Erickson et al., 2010; Li et al., 2014a,b; Wu et al., 2013). Unfortunately, these methods require labeled antibodies for the assay readouts, incurring high cost and additional stap in performing the assay. They possess some other limitations such as low sensitivity, poor reproducibility, and time-consumption. Search for high sensitive and selective, affordable and label-free techniques in cancer diagnosis is still ongoing to replace the existing methods.

* Corresponding author.
** Corresponding author.,
*** Corresponding author.
E-mail addresses: wangyychem@mail.scuec.edu.cn (Y. Wang), lichychem@mail.scuec.edu.cn (C. Li), nianjun.yang@uni-siegen.de (N. Yang).

https://doi.org/10.1016/j.bios.2019.111540
Received 16 April 2019; Received in revised form 24 July 2019; Accepted 25 July 2019
Available online 26 July 2019
0956-5663/

Photoelectrochemical (PEC) immunosensing system is one promising technological platform, which possesses superior features such as high sensitivity, low cost, simple instrumentation, and great potential for miniaturization (Ibrahim et al., 2018; Li et al., 2018; Tan et al., 2017; Xu et al., 2018). Past studies have demonstrated that PEC sensors exhibit high sensing performances towards biomacromolecule and bioactive small molecules (Tada et al., 2011; Zhang et al., 2019) as well as clinical diagnostics (Golub et al., 2009; Yang et al., 2018). To construct PEC immunosensors (Hagfeldt et al., 2010; Yu et al., 2015), bioactive elements (usually antibodies) are often immobilized onto the photoelectrochemical interface for specific recognition of target molecules in a biological sample. During the assay development, the target molecules (commonly antigens) are bound to the sensing interface through immunoreaction (Ye et al., 2018), and thus causing the change of the photocurrent response which can be ultilized as the readout signals for the determination of antigens (Tan et al., 2017). Due to the fact that the energy form of readout signal as current in PEC platform is completely different from the energy form of the excitation source such as visible light, the PEC sensing system affords ultralow background signal, which makes the PEC sensing ultrahigh sensitive (Li et al., 2018; Xu et al., 2018). Compared with traditional immunoassays, additional benefits for a PEC immunosensors include label-free analysis and inexpensive instrumentation.

The heart of PEC immunosensors is the photoelectric conversion materials. The currently used photoelectric conversion materials for PEC sensors are mainly wide-band-gap inorganic semiconductors such as TiO_2, ZnS QDs, and CdS QDs, etc. To excite these photoactive materials and generate photocurrents, a bulky, expensive high-energy excitation source is the typical strict requirement. But, biological sensing elements can be easily deactivated with high-energy illumination, ultimately resulting in poor sensing performances. Besides, the photoconversion efficiencies of these photoactive materials are still relatively low. Therefore, developing novel photoactive materials with excellent photoelectrochemical properties will allow significant breakthrough for PEC sensing system.

Metal-organic frameworks (MOFs) are very attractive alternative materials for PEC immunosensor fabrication. MOFs are self-assembled through coordination and covalent bonding between the bi-dentate or multi-dentate organic ligands and central metal ions (Silva et al., 2015; Zhou and Kitagawa, 2014). They possess highly repetitive units, network-like structures with high porosity, and large specific surface area ideally for gas adsorption/separation, catalysis, purification, energy storage and conversion (Huang et al., 2017; Liu and Tang, 2013; Rodenas et al., 2015; Tian et al., 2018; Wang et al., 2016; Xia et al., 2015; Zhao et al., 2017). Recently, there are upsurging studies on the synthesis and the applications of multi-functional MOF (Cao et al., 2009; Jiang et al., 2011; Jiang and Xu, 2011; Liu and Tang, 2013). But most of the attempts show less progress in the utilization of MOF for PEC sensing platform as most of the developed MOFs has low photoelectric conversion efficiency, poor conductivity as well as poor long-term stability in aqueous solution.

Herein, an ionic liquid based Zn-MOF was synthesized and used as a photoactive element for the label-free PEC immunosensing of SCCA. To enhance the photoelectric conversion efficiency of Zn-MOF, the spatial confinement growth of gold nanoparticles (Au-NPs) in the nanopores of Zn-MOF was accomplished by *in-situ* reduction of $HAuCl_4$ with acetic acid. Au-NPs@Zn-MOF was further functionalized with 1*H*-imidazolium-1,3-bis(2-aminoethyl)bromide (IBABr) ionic liquid, and then employed as a photoelectrochemical interface for immobilizing anti-SCCA and fabricating a PEC immunosensor. The characterizations of Au-NPs@Zn-MOF, as well as its PEC sensing performances towards SCCA, were thoroughly investigated.

2. Experimental section

2.1. Materials and apparatus

1,3-Dibromopropane, methyl 4-bromobenzoate, imidazole, and 2-bromoethylamine hydrobromide were bought from Shanghai Aladdin Reagent Inc. (Shanghai, China). N-(Trimethylsilyl) potassium hydroxide, hydrochloric acid, ascorbic acid (AA), $Zn(NO_3)_2.6H_2O$, $AuCl_3{\cdot}3H_2O$, and glutaraldehyde (GLD) (25% aqueous solution) were purchased from Sinopharm Chemical Reagent Co., Ltd (Shanghai, China). Squamous cell carcinoma antigen (SCCA) and monoclonal (Mouse) primary anti-human SCCA antibody (anti-SCCA) were obtained from Linc-Bio Science Co. (Shanghai, China). Bovine serum albumin (BSA), glutamic acid (Glu), and Glycine (Gly) were bought from Shanghai Ruji Biotechnology Co., Ltd (Shanghai, China). Neuron Specific Enolase (NSE) was bought from Beijing Biosynthesis Biotechnology Co., Ltd (Beijing, China). Immunoglobulin G (IgG) was acquired from Beijing Solarbio Science & Technology Co., Ltd (Beijing, China). α-fetoprotein (AFP) was acquired from Beijing Biosynthesis Biotechnology Co. Ltd (Beijing, China). Human serum albumin (HSA) was provided by Shanghai Pufei Biotech Co. Ltd (Shanghai, China). All other reagents were of analytical grade and were used as received. All solutions were prepared by using ultra-pure water. Human serum samples were kindly supplied by Renmin Hospital of Wuhan University (Wuhan, China).

The FTIR analysis was carried out with a Nicolet IS10 FTIR spectrometer (Thermo Nicolet, USA). Fluorescence spectrum was collected on a Hitachi F-7000 fluorescence spectrophotometer (Hitachi, Japan). The UV–vis DRS was conducted on a Shimadzu UV-2600 UV–Vis spectrophotometer using $BaSO_4$ as the reference. ^{1}H NMR spectrum was obtained from AVANCE III 400 NMR system (Bruker, German). HPLC–MS analysis was conducted on an Agilent G6520 Q-TOF liquid chromatograph-mass spectrometer (Agilent, USA). Transmission electron microscopy (TEM) images were obtained from a FEI Tecnai G^2 20S-TWIN instrument (FEI Company, Netherlands) at an acceleration voltage of 200 kV. XPS analysis was performed on a MULT1LAB2000 X-ray photoelectron spectrometer (XPS) (VG, USA). Scanning electron microscopy images were recorded on a JEOL-6700F instrument (JEOL Ltd, Japan) with the electron beam voltage of 15.0 kV. The porosity and total surface area of as-synthesized materials were determined by N_2 adsorption-desorption isotherms using a Micromeritics TriStarII3flex system (Micromeritics, America). A 405 nm LED lamp (150 mW) was used as the excitation light source. The light intensity (about 150 mW cm^{-2}) was measured with a radiometer (Photoelectric Instrument Factory of Beijing Normal University, Beijing, China). Electrochemical measurements were obtained on CHI 920D electrochemical workstation (Chen Hua Corp., Shanghai, China), where a L-shaped glassy carbon electrode (GCE) with a diameter of 3 mm was used as the working electrode, a Pt wire as a counter electrode, and a saturated calomel electrode (SCE) as the reference electrode. All the photocurrent measurements were obtained at a constant potential of 0.15 V (*vs.* SCE) in a 0.1 M pH 7.0 phosphate buffer containing 0.15 M ascorbic acid (AA) at room temperature. Electrochemical impedance spectroscopy (EIS) was measured in a 0.1 M KCl solution containing 5.0 mM $K_3[Fe(CN)_6]/K_4[Fe(CN)_6]$ (1:1). The initial potential was the average value of the redox peak potentials (0.2 V *vs.* SCE) with an amplitude of 5 mV over a frequency range of 100 mHz to 100 kHz.

2.2. Synthesis of $PDBCBIm(PF_6)_2$ ionic liquid

The synthesis process of $PDBCBIm(PF_6)_2$ ionic liquid is shown in Scheme S1. In the first step, 2.0 g of 4-(1H-azol-1-ylmethyl) benzoate (or 9.25 mmol) was dissolved in 30 mL of acetonitrile and then dropwise added to a mixed solution of 1, 3-dibromopropane (0.935 g, 4.625 mmol) and acetonitrile (20 mL). The mixture was refluxed for 48 h with constant stirring to complete the reaction. The solvent was

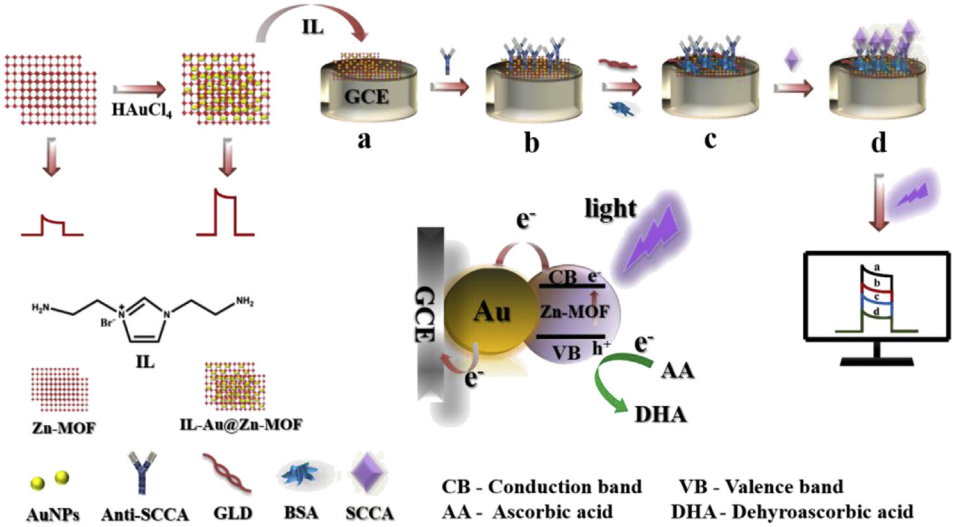

Scheme 1. The overall fabrication process of the PEC immunosensor and the specific response to SCCA, and the mechanism for the photocurrent generation.

then removed by vacuum suction filtration. The filtrate was thoroughly washed with acetonitrile to yield a pale-yellow solid product. The dried product was transferred to a saturated ammonium hexafluorophosphate solution to produce a white precipitate immediately. The mixture was stirred at 50 °C for 5 h, and subsequently separated by filtering. The crude product was thoroughly washed with ultrapure water. Then, the product was re-dissolved in the mixture of ethanol and ultrapure water (v/v = 4:1). KOH was added to the product solution successively. After being reacted at 80 °C for 4 h, the mixture solution was cooled to room temperature. The pH value of the solution was adjusted to 2.0 by adding HCl solution while maintaining the reaction mixture at room temperature. Subsequently, the mixture was separated by vacuum filtration and the crude product was washed with ultrapure water, and dried under vacuum to give the desired product: $PDBCBIm(PF_6)_2$ ionic liquid (yield: 64.8%). The product was characterized by ^{1}H-NMR, FT-IR and HPLC-MS. All results are shown in Figure S 1.

2.3. Synthesis of IBABr ionic liquid

Methyl-4-(1H-azol-1-ylmethyl) benzoates and 1*H*-imidazolium-1,3-bis(2-aminoethyl)bromide ionic liquid were synthesized according to the previous reports with minor modifications (Zhou et al., 2019). The chemical structure of 4-(1H-azol-1-ylmethyl) benzoate was confirmed by ^{1}H NMR spectra. The result was shown in Figure S 2.

2.4. Synthesis of Zn-MOF

A mixture of $Zn(NO_3)_2.6H_2O$ (80.8 mg, 0.27 mmol), $PDBCBIm(PF_6)_2$ ionic liquid (200 mg, 0.27 mmol) and DMF (32 mL) was heated in a Teflon-lined stainless vessel at 160 °C for 48 h. After cooling this mixture down to ambient temperature, yellow crystals (Zn-MOF) were separated by filtration, purified, and dried under vacuum. The yield ratio was about 40%.

2.5. Synthesis of Au-NPs@Zn-MOF nanocomposite

In a mixture of ultrapure water (9.2 mL) and glacial acetic acid (0.8 mL), 20 mg of $HAuCl_4.4H_2O$ was dissolved. Zn-MOF was treated in vacuum to produce a negative pressure in the nanopores. The $HAuCl_4$ solution was injected into the sealed system. The mixture was kept in an ice bath for 3 h in air. Subsequently, Zn-MOF was separated from the mixture at a centrifugation rate of 1500 rpm for 10 min. After that, the acetic acid solution was mixed with Zn-MOF. A reaction time of 14 h and a reaction temperature of 35 °C were applied. Finally, the solid product was separated with centrifugation at a speed of 1500 rpm and thoroughly washed with ultrapure water, and dried in vacuum to yield Au-NPs@Zn-MOF nanocomposite.

2.6. Synthesis of IBABr functionalized Au-NPs@Zn-MOF

In 10 mL of ultrapure water, 20 mg of Au-NPs@Zn-MOF was dispersed in an ice bath. The mixture was sonicated for 2 h to weaken the interlayer interaction of Zn-MOF and allow Au-NPs to be well integrated on Zn-MOF to yield Au-NPs@Zn-MOF nanocomposites with thin-layer structure and small size. Then, 70.5 mg of IBABr was added to Au-NPs@Zn-MOF solution and gently stirred at 35 °C for 24 h to accomplish the functionalization procedure. Finally, the mixture was centrifuged at a speed of 5000 rpm for 10 min. After the excess reagents were removed, the residual solid material was washed thoroughly with ultrapure water, and dried in vacuum. The IBABr-Au-NPs@Zn-MOF nanocomposite was dispersed in ultrapure water to give a suspension solution (0.5 mg mL^{-1}).

2.7. Fabrication of PEC immunosensors

A polished and clean L-shaped GCE (Φ = 3 mm) was drop coated with 6.0 μL of 0.5 mg mL^{-1} IBABr-Au-NPs@Zn-MOF suspension. To provide a platform for the immobilization of SCCA antibody, 5 μL of 5.0 μg mL^{-1} anti-SCCA solution was then drop-coated onto the surface of the IBABr-Au-NPs@Zn-MOF/GCE. After being kept at 35 °C for 1 h, the physically absorbed residues were removed by gently stirring in a phosphate buffer. Subsequently, the electrode surface was exposed in a vial containing glutaraldehyde vapor for a cross-linking process to covalently immobilize anti-SCCA on the nanocomposite. An incubation process by soaking the electrode in a BSA solution (0.25%) was run for 30 min with gentle stirring to block the residual aldehyde groups. Followed by thorough washing with phosphate buffer, a PEC immunosensor for the SCCA detection was fabricated. Prior to SCCA measurements, the anti-SCCA(BSA)/IBABr-Au-NPs@Zn-MOF/GCE was incubated in SCCA solutions with different concentrations at 35 °C for 30 min. The overall fabrication process of the Au-NPs@Zn-MOF based immunosensor and the PEC determination of SCCA is illustrated in Scheme 1.

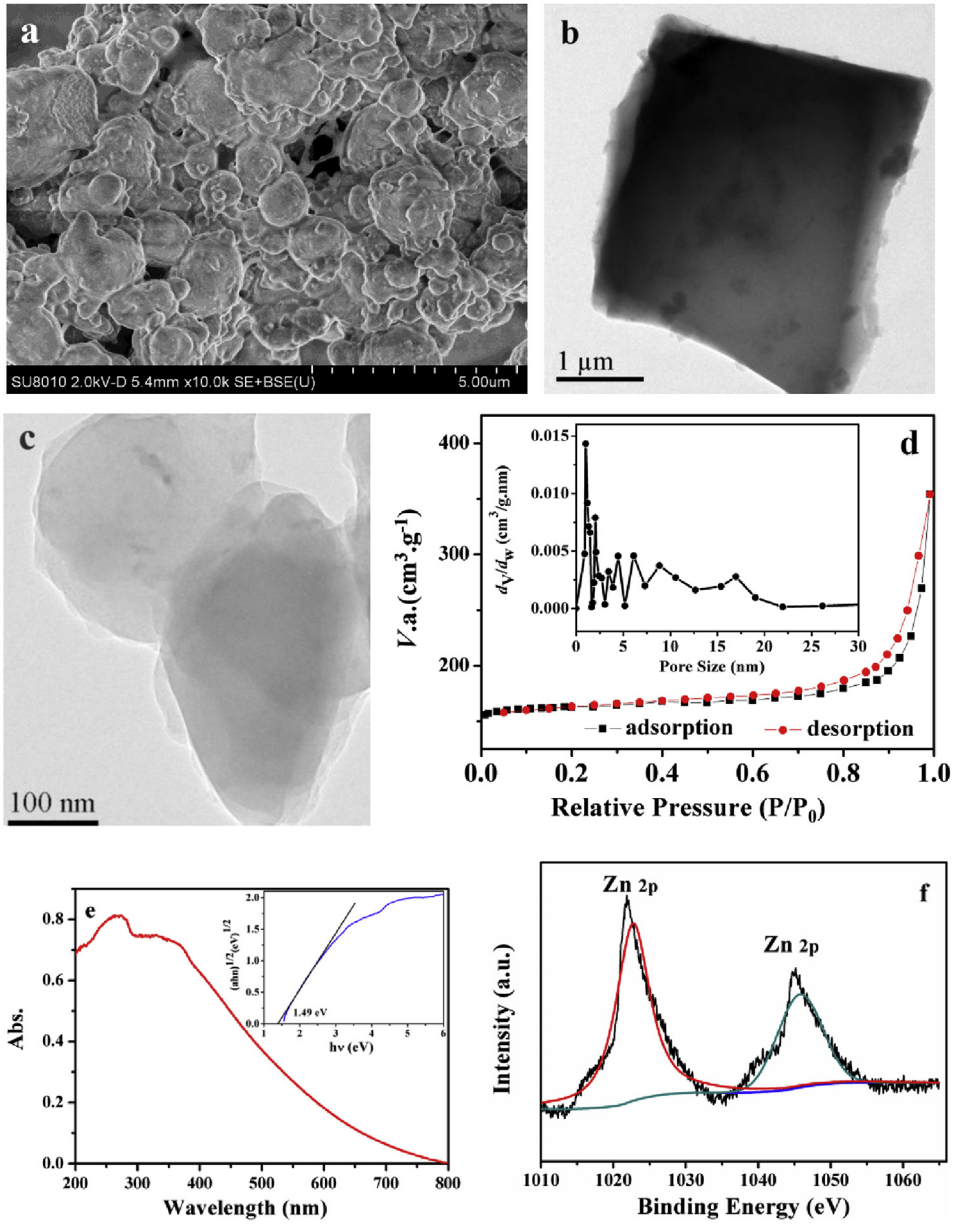

Fig. 1. SEM image of Zn-MOF bulk crystals (a), TEM images of single Zn-MOF bulk crystal (b) and Zn-MOF nanosheets (c); Nitrogen adsorption/desorption isotherm at 77 K for Zn-MOF nanosheets (d), Diffuse reflective spectra (DRS) of Zn-MOF nanosheets (e); detailed XPS spectra of Zn 2p (f).

3. Results and discussion

3.1. Construction of PEC immunosensors

As-synthesized Zn-MOF and Au-NP@Zn-MOF were characterized by electron microscopy, nitrogen adsorption/desorption isotherm analysis, diffuse reflective spectra (DRS), and X-ray photoelectron spectroscopy (XPS). Fig. 1 a presents the scanning electron microscopy (SEM) image of the Zn-MOF nanocomposites, revealing their irregular shape. The size of these Zn-MOF crystals varied from hundreds of nanometers to several micrometers. The transmission electron microscopy (TEM) image of a single Zn-MOF (Fig. 1 b) indicates that the typical Zn-MOF crystal has clear edges. Its thickness is about 135 nm too thick to possess good photoelectric conversion efficiency. An exfoliation process was further applied, namely exfoliation of the dispersed Zn-MOF bulk crystals in water by ultrasonication. The TEM image of the as-exfoliated Zn-MOF is shown in Fig. 1 c, where the thickness and the size of the exfoliated Zn-MOF are estimated in the range of nanometers. The Zn-MOF nanosheets provide more active sites and lead to higher photoelectric conversion efficiency than Zn-MOF bulk crystals. The specific surface area of Zn-MOF nanosheets was then measured using nitrogen adsorption/desorption isotherms. The specific surface area and pore volume calculated using the Brunauer-Emmett-Teller (BET) equation are 480 $m^2 g^{-1}$ and 0.299 $cm^3 g^{-1}$, respectively (Fig. 1 d), suggesting the synthesized nanosheets are suitable to immobilize sensing/target molecules (e.g., antibodies) and the nanopores are accessible as pockets to embed additional functional materials (e.g., metal NPs). Therefore, the application of Zn-MOF nanosheets as the sensing material is expected to improve sensing performance. To further confirm the enhanced photoelectrochemical property of these Zn-MOF nanosheets for PEC sensing applications, its bandgap was estimated from their diffuse reflective spectra (DRS). These Zn-MOF nanosheets are semi-conductive and have a bandgap of 1.49 eV (Fig. 1 e). The detailed X-ray photoelectron spectrum (XPS) of Zn-MOF (Fig. 1 f) exhibits two peaks at ~1022 and ~1045 eV, which are assigned to Zn $2p_{3/2}$ and Zn $2p_{1/2}$, respectively.

To further clarify the chemical structure of Zn-MOF nanosheets, their IR spectrum was recorded (Fig.S 3a). A broad peak appearing at 3416 cm^{-1} is due to water molecules. The peaks at 1611 and 3049 cm^{-1} are attributed to the C=O and C–H stretching of coordinated DMF molecules, respectively. The asymmetric stretching vibration of the chelating nitrate is observed at 1160 cm^{-1}. The recorded fluorescence spectrum of Zn-MOF (Fig.S 3b) exhibits a strong emission peak at 460 nm with an absorption peak at 372 nm. It is distinctively different from the spectrum of the ionic liquid where shows a strong emission peak at 297 nm with an excitation peak at 250 nm. The red-shift on emission wavelength mainly comes from the strong electronic coupling between the ligands and metal central ions. The chemical compositions of Zn-MOF nanosheets were then characterized by TEM-EDAX, revealing the presence of expected elements (Fig.S 4a). All above results illustrate unambiguously that Zn-MOF nanosheets consist of zinc ion metal center and the ligand of as-synthesized ionic liquid with a nanoporous structure that offers regularly segregated sites to load metal nanoparticles (e.g., Au NPs).

Au NPs were then embedded into these Zn-MOF nanosheets by means of an *in-situ* reduction approach. The TEM images of Au-NPs@Zn-MOF are shown in Fig. 2 a where the uniform distribution of particles (black dots) is clearly visible on the entire surface of Zn-MOF nanosheets. A higher resolution TEM image (Fig. 2 b) confirms the embedding of these nanoparticles in a well-arranged manner. SEM elemental mapping images, shown in Figure S 5, confirm the homogeneous distribution of Au, Zn, C, N and O elements throughout the entire Au-NPs@Zn-MOF nanocomposite, demonstrating the successfully integrated AuNPs within Zn-MOF. The size of gold particles is smaller than 4 nm and their average size is about 2.82 nm (Fig. 2 c). The specific surface area and total pore volume of Au-NPs@Zn-MOF, measured using N_2 adsorption/desorption isotherms (Fig. 2 d) are reduced to 137 $m^2 g^{-1}$ and 0.11 $cm^3 g^{-1}$, respectively. The existence of Au NPs

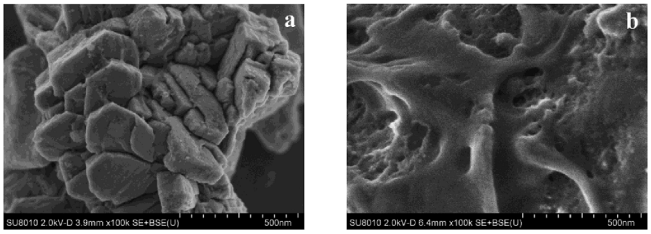

Fig. 3. SEM images of IBABr-Au-NPs@Zn-MOF/GCE (a) before and (b) after the immobilization of anti-SCCA and BSA.

inside Zn-MOF is further confirmed by their XPS analysis (Fig. 2 e) where $Au4f_{7/2}$ at a binding energy of 84.8 eV and $Au4f_{5/2}$ at a binding energy of 87.5 eV are clearly noticed. The positive shift in the binding energy of Au $4f_{7/2}$ results from the electronic effect of small-sized particles. Chemical compositions of Au-NPs@Zn-MOF analyzed by TEM-EDAX (Figure S 4b) confirm the results of XPS analysis. Therefore, *in-situ* spatial confinement growth of Au NPs is achieved in the pores of Zn-MOF nanosheets. Such a nanocomposite features a large surface area as well as uniform size and well-distributed active centers. This is doable because the spatially confined and well-reproduced pores inside MOF are actually templates that inhibit the aggregation and migration of Au NPs (Jiang et al., 2011; Jiang and Xu, 2011). Au-NPs decorated Zn-MOF (Au-NPs@Zn-MOF) nanocomposites are thus able to accelerate the transfer rate of photogenerated carriers and improve greatly the separation of electron-hole pairs, eventually leading to enhanced photoelectric conversion efficiency. Au-NPs@Zn-MOF nanocomposites are thus promising as photoactive elements for the PEC sensors.

To construct a PEC immunosensor for the detection of SCCA, Au-NPs@Zn-MOF nanocomposites were further modified with IBABr ionic liquid. Using this linker, anti-SCCA was then immobilized on the

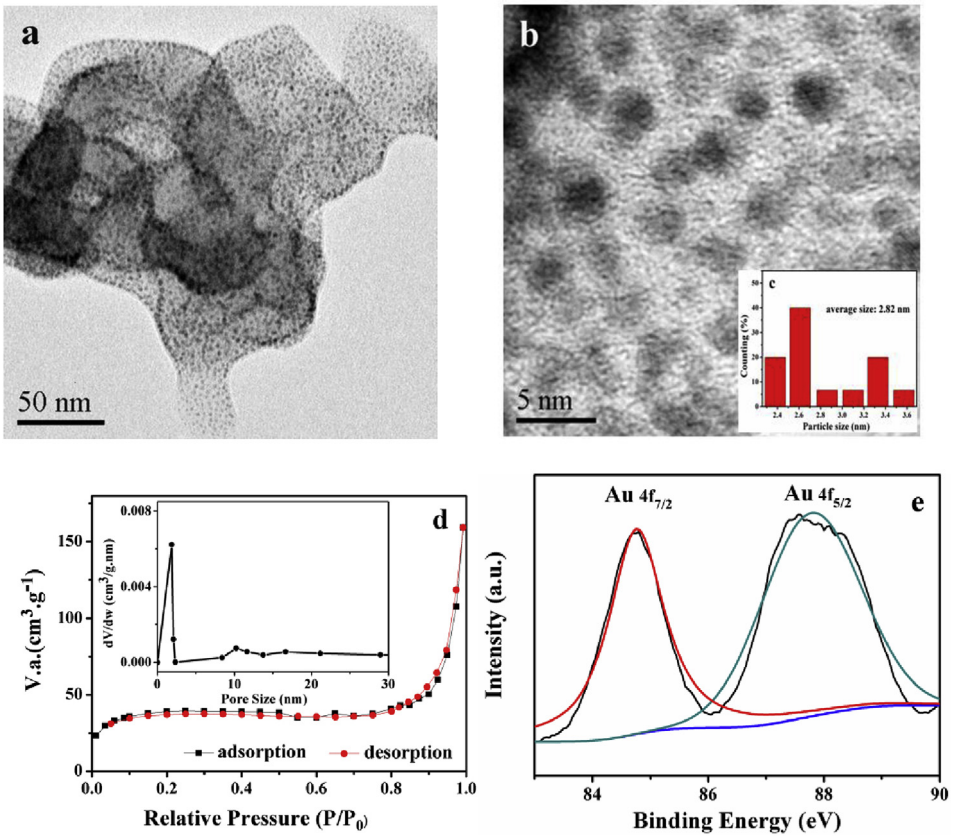

Fig. 2. TEM images of Au-NPs@Zn-MOF at different resolutions (a, b), Size distribution of Au NPs inside the pores of Zn-MOF nanosheets (c), Nitrogen adsorption/desorption isotherm of Au-NPs@Zn-MOF (d); XPS spectra of Au 4f (e).

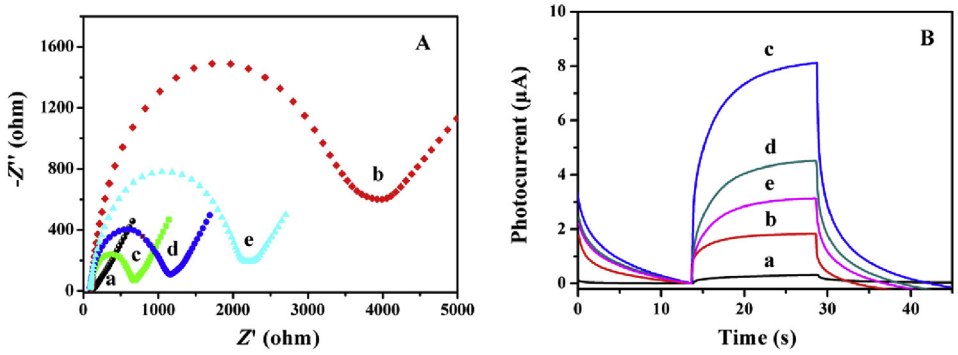

Fig. 4. (A) Nyquist plots and (B) photocurrent responses of a GCE(a), a Zn-MOF/GCE (b), an IBABr-Au-NPs@Zn-MOF/GCE (c), an anti-SCCA(BSA)/IBABr-Au-NPs@Zn-MOF/GCE) (d), and a SCCA/anti-SCCA(BSA)/IBABr-Au-NPs@Zn-MOF/GCE (e). For (A), 5 mM $K_3Fe(CN)_6$/$K_4Fe(CN)_6$ in 0.1 M KCl solution was used. In (B), the solution of 0.15 M ascorbic acid and a potential of 0.15 V were used; SCCA concentration was 1.0 ng mL^{-1}.

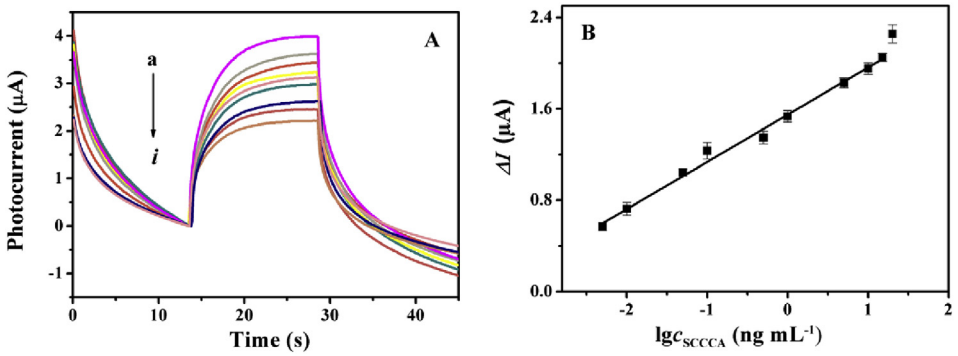

Fig. 5. (A) Chronoamperometric curves of an anti-SCCA(BSA)/IBABr-Au-NPs@Zn-MOF/GCE towards the detection of SCCA at the concentration of (a) 0.005, (b) 0.01, (c) 0.05, (d) 0.1, (e) 0.5, (f) 1.0, (g) 5.0, (h) 10.0, and (i) 15.0 ng mL^{-1}); (B) the calibration curve for the SCCA determination using an anti-SCCA(BSA)/IBABr-Au-NPs@Zn-MOF/GCE.

surface of IBABr-Au-NPs@Zn-MOF/GCE. The SEM image of the surface of an IBABr-Au-NPs@Zn-MOF layer (Fig. 3 a) shows many nanosheets with irregular shape, distributed densely on the surface of a glassy carbon electrode (GCE). After the subsequent immobilization of anti-SCCA and bovines serum albumin (BSA), the surface morphology changes significantly (Fig. 3 b). A glue-like and thick layer can be seen. This is because of the covalent cross-linking reaction of the amino groups between IBABr-Au-NPs@Zn-MOF and anti-SCCA (or BSA), enabling the stable immobilization of anti-SCCA on the surface of IBABr-Au-NPs@Zn-MOF to form a sensing platform, namely anti-SCCA(BSA)/IBABr-Au-NPs@Zn-MOF/GCE.

The interfacial properties of the sensing platforms were investigated using electrochemical impedance spectroscopy (EIS) during the course of the stepwise fabrication of anti-SCCA(BSA)/IBABr-Au-NPs@Zn-MOF/GCE. By using $K_3Fe(CN)_6$/$K_4Fe(CN)_6$ as redox probes, the charge transfer resistance (R_{ct}) was estimated from the diameter of the semicircle in the Nyquist plot at higher frequencies. Fig. 4 A compares the Nyquist plots of a GCE (a), a Zn-MOF/GCE (b), an IBABr-Au-NPs@Zn-MOF/GCE (c), an anti-SCCA(BSA)/IBABr-Au-NPs@Zn-MOF/GCE (d), and a SCCA/anti-SCCA(BSA)/IBABr-Au-NPs@Zn-MOF/GCE (e). The equivalent circuit (Figure S 6) was applied to calculate their R_{ct} values with the aid of a ZSimDemo software. The introduction of Zn-MOF nanosheets onto a GCE leads to an increase of R_{ct} from 40.2 Ω to 3472.0 Ω. This indicates that Zn-MOF nanosheets hinder the electron transfer of redox probes to the electrode surface significantly. Once Au NPs and IBABr ionic liquid being integrated onto Zn-MOF nanosheet, the R_{ct} value decreases to 565.6 Ω. In other words, both Au NPs and IBABr facilitate the electron transfer of $K_3Fe(CN)_6$/$K_4Fe(CN)_6$. After the immobilization of anti-SCCA and BSA onto the IBABr-Au-NPs@Zn-MOF, the R_{ct} value increases again due to the limiting transport of redox probe to the electrode surface (Fig. 4A d). The increasing variation of R_{ct} values concludes the successful immobilization of anti-SCCA on these interfaces. As expected, once a process for the specific recognition of SCCA is accomplished, the R_{ct} value is further increased (Fig. 4A e). Note that, in Fig. 4A (d) (namely in the last step of immunosensor fabrication), unoccupied active sites were eliminated by their crosslinking with BSA. Therefore, the reduction of this photocurrent originates from bonded SCCA. The variation of this photocurrent can be utilized for the determination of SCCA.

In this unique PEC sensing system, ascorbic acid was chosen as an electron donor because ascorbic acid is known to be efficient to capture photo-generated holes, prohibit the electron-hole pair recombination, and facilitate the generation of photocurrent. As a control experiment and without the photoactive interface, a GCE has no current response in 0.15 M ascorbic acid shown in Fig. 4B a. After Zn-MOF nanosheets were coated onto the GCE surface, the photocurrent response significantly increases to ~2 μA (Fig. 4B, b) in 0.15 M ascorbic acid. This photocurrent was further enhanced to ~8 μA after the introduction of IBABr and Au NPs (Fig. 4B c). This demonstrates the excellent properties of IBABr ionic liquid and Au NPs on improving the photoelectrochemical conversion efficiency of Zn-MOF nanosheets. There are three factors contributing to the enhancement of the PEC response on this unique photoactive interface, which are crucial to the success of ultrasensitive detection of cancer biomarkers. First, conductive IBABr ionic liquid and Au NPs promote the transfer of photogenerated carriers and reduce the chance for the recombination of carriers to generate photocurrent. Second, the surface plasmon resonance effect of Au NPs can contribute the increase in photocurrent response (Ye et al., 2018; Luo et al., 2018). Third, a large specific surface area of Zn-MOF nanosheets and the excellent biocompatibility of Au NPs supply abundant active sites to immobilize anti-SCCA. Upon anti-SCCA being immobilized and SCCA being specifically captured, the photocurrent response decreases successively, as shown in Fig. 4 B curve d and e, respectively. This decrease in photocurrent arises from the blocking effect of proteins to the transfer of photogenerated electron and the mass transfer of ascorbic acid, achieving the signal off PEC immunosensing platform for the determination of SCCA. The sensing performance of a PEC immunosensor based on Zn-MOF was also investigated. As presented in Fig. S 7, for sensing of 1.0 ng mL^{-1} SCCA, the photocurrent variation is significantly lower than that obtained at the PEC immunosensor based on Au-NPs@Zn-MOF, indicating the importance of the in-situ formation of Au-NPs within Zn-MOF.

Table 1
Comparision of the analytical characteristics of the Au-NPs@Zn-MOF based PEC immunosensor with the previously reported sensors.

Methods	Materials	Linear range (ng mL^{-1})	Detection (pg mL^{-1})	Reference
Photoelectrochemical immunosensor	IBABr-Au-NPs@Zn-MOF	0.005 - 15	2.34	This work
Electrochemical detection	reduced graphene oxide-tetraethylene pentamine nanocomposite	0.03 - 20	10.0	Wu et al. (2014)
Cathodic electrochemiluminescence immunosensor	Carboxylated g-C_3N_4 and graphene nanocomposite	0.025 - 10	8.53	Li et al. (2014a)
Nonenzymatic immunosensor	bimetallic gold-silver nanoclusters	0.005 -20	1.3	Zhang et al. (2014)
Immunosensor based on electrochemiluminescence resonance energy transfer	CdTe@Carbon dots nanocomposite	0.02 -12	6.3	Li et al. (2014b)
Electrochemical immunosensor	Lmellar montmorillonite-gold nanostructures	0.001 - 5	0.3	Jia et al. (2015)
Electrochemical immunosensor	ternary Pt/PdCu nanocube anchored on three-dimensional graphene framework	0.0001 -30	25	Liu et al. (2016)
Electrochemical immunosensor	Co_3O_4@CeO_2–Au@Pt nanocomposite	0.0001 - 80	33	Li et al. (2017a)
Electrochemical immunosensor	Icosahedral gold nanocrystals and DMIB ionic liquid	0.02 - 10	12.6	Li et al. (2017b)

3.2. Performances of PEC immunosensors

Experimental conditions were optimized to result in a high photocurrent variation for the SCCA determination, primarily the concentration of ascorbic acid and incubation time. The photocurrent response increases with the concentration of ascorbic acid (Figure S8 a) and 0.15 M of ascorbic acid is the best for immunosensing 1.0 ng mL^{-1} SCCA. In detail, the photocurrent increases as the concentration of ascorbic acid increasing from 0 to 0.15 M, and reaches a maximum value at the concentration of 0.15 M. Higher concentration than 0.15 M leads to a declined on the photocurrent, an indication of a hindering effect of ascorbic acid on the electron transfer (Tan et al., 2018). Regarding incubation time, the photocurrent increases with the incubation time within 30 min and then reaches a plateau after 30 min (Figure S 8b). An incubation time of 30 min in the SCCA solution was then applied for further studies.

Under the optimized operating conditions, the quantitative analysis of SCCA was conducted on the PEC immunosensing interface. Fig. 5 A presents the *i-t* curves of anti-SCCA(BSA)/IBABr-Au-NPs@Zn-MOF/GCEs toward the detection of SCCA, of which the SCCA concentration was varied from 5.0 pg mL^{-1} to 15.0 ng mL^{-1}. The photocurrent decreases when the SCCA concentration increases. The photocurrent variation ($\Delta I = I_0 - I$, I_0 and I are the photocurrents of the anti-SCCA/IBABr-Au-NPs@Zn-MOF/GCE before and after being interacted with SCCA, respectively) reflects the rebinding of SCCA on this immunosensor and is found to be linear with the logarithm of SCCA concentration [lgc_{SCCA} (ng mL^{-1})] in the investigated concentration range, following the equation of $\Delta I = 0.414\ lgc_{SCCA}$ (ng mL^{-1}) + 1.55 ($R^2 = 0.998$) (Fig. 5 B). The calculated detection limit is 2.34 pg mL^{-1} (S/N = 3). The performance comparison of this PEC immunosensor with those previous reports (in Table 1) confirms the comparability of the as-prepared PEC immunosensor to other sensors in terms of the working linear range and detection limit.

The specificity of the assembled PEC immunosensor is another important study, which was carried out in the presence of potential interferents in human serum. Each sample containing 1.0 ng mL^{-1} SCCA and 10.0 ng mL^{-1} interferent such as immunoglobulin G (IgG), human serum albumin (HSA), alpha fetoprotein (AFP), neuron specific enolase (NSE), glucose (Glu) and glycine (Gly) was investigated independently. The study found all interferent samples produce photocurrent not significantly different than the photocurrent response of the sample containing 1.0 ng mL^{-1} SCCA alone. In fact, the deviation of the obtained photocurrent is only in the range of −2.6%–6.5% (Fig. 6 a). Furthermore, the photoelectrochemical responses of the PEC immunosensor towards SCCA, IgG, HAS, AFP, NSE, Glu and Gly at the concentration of 1.0 ng mL^{-1} were also investigated independently. As shown in Figure S 9, the photocurrent variation for the interaction with SCCA is significantly larger than that for other biomolecules. All results indicate that the anti-SCCA(BSA)/IBABr-Au-NPs@Zn-MOF based PEC immunosensor possesses high selectivity towards SCCA detection.

The physical adsorption of SCCA on the sensing interface was evaluated by comparing the photocurrent response of the Au-NPs@Zn-MOF/GCE before and after being interacted with SCCA. As shown in Figure S 10, no significant photocurrent variation was observed, indicating the amount for the physical adsorption of SCCA onto the Au-NPs@Zn-MOF/GCE surface can be neglected.

Stability and reproducibility of the sensor are other two important aspects before its practical use. To evaluate the stability of an IBABr-Au-NPs@Zn-MOF/GCE, visible light was used to illuminate this interface at a pulse period of 15 s for 20 cycles. As shown in Fig. 6 b, no significant variation is observed on the photocurrent response, indicating the IBABr-Au-NPs@Zn-MOF/GCE is stable under the illumination of the visible light. To study the long-term stability of this PEC immunosensor, the anti-SCCA(BSA)/IBABr-Au-NPs@Zn-MOF/GCE was stored at 4 °C for two weeks before it was re-used to determine 1.0 ng mL^{-1} SCCA. The photocurrent was only 5.6% lower than that obtained before such

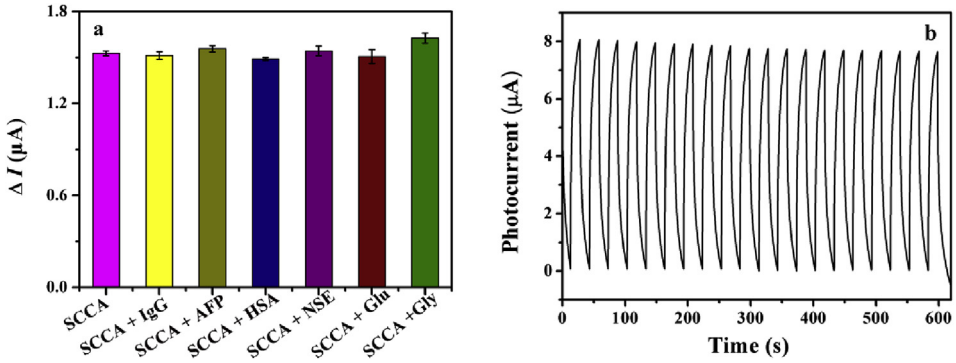

Fig. 6. Photoelectrochemical responses of the PEC immunosensor towards 1.0 ng mL^{-1} of SCCA in the absence and presence of 10 ng mL^{-1} of IgG, HAS, AFP, NSE, Glu and Gly (a); Photocurrent response of an IBABr-Au-NPs@Zn-MOF/GCE under successive illumination (b).

storage. Thus, the IBABr-Au-NPs@Zn-MOF/GCE has good long-term stability. The fabrication reproducibility was evaluated by comparing the photocurrents obtained on six independently prepared anti-SCCA(BSA)/IBABr-Au-NPs@Zn-MOF/GCEs towards the detection of 1.0 ng mL^{-1} SCCA. The relative standard deviation of recorded photocurrents is only 5.4%.

After studies on the merits of the PEC immunosensor, it was further used to determine SCCA concentration in clinical serum samples. To evaluate the accuracy of this PEC immunosensor, the same set of samples was also assayed with ELISA method. By ELISA method, the estimated SCCA concentrations in clinical serum samples are 0.40, 1.17, 2.62, and 4.13 nm mL^{-1}. The reading from PEC immunosensor for the same samples is 0.38, 1.20, 2.57, and 4.25 ng mL^{-1}, respectively. The relative standard deviations for different concentrations of SCCA in the clinical serum samples are −5.0%, 2.56%, −1.91% and 2.91%, respectively. Overall, the study suggests that the developed PEC immunosensor exhibits highly sensitivity and selectivity, long-term stability, and good reproducibility towards the detection of SCCA. It can be applied as a label-free device for the SCCA determination.

4. Conclusions

Photoresponsive Zn-MOF has been synthesized using carboxyl functionalized ionic liquid as ligand and zinc ion as the metal center. Zn-MOF features large surface area and highly porous structure, creating periodic spatially confined pockets with uniform dimension for the in-situ loading of gold nanoparticles. Such Au-NPs@Zn-MOF nanocomposite enhances the photocurrent response of Zn-MOF under visible light illumination. After being functionalized with IBABr ionic liquid, Au-NPs@Zn-MOF based sensing platform was used to immobilize anti-SCCA to construct a highly sensitive, selective, stable, and reproducible photoelectrochemical immunosensor for SCCA assay. This study provides a new strategy for implementing photoresponsive metal organic framework materials with high photoelectrochemical conversion efficiency to the development of an efficient platform for fabricating photoelectrochemical biosensors. Although gold nanoparticles can be spatially confined in Zn-MOF and help to improve the photoelectrochemical sensing performances, the procedure for this nanocomposite is complex, and is difficult to characterize the in-situ producing gold nanoparticles and the mechanism for enhancing the photocurrent response. The practicability of the immunosensor in diagnosis, prognosis evaluation, and monitoring treatment process of tumors is still filled with challenges.

Declaration of competing interest

The authors declare that they have no known competing financial interests or personal relationships that could have appeared to influence the work reported in this paper.

CRediT authorship contribution statement

Qiuxi Wei: Methodology, Writing - original draft. **Chen Wang:** Formal analysis, Software. **Xue Zhou:** Validation. **Tsunghsueh Wu:** Writing - review & editing. **Yanying Wang:** Conceptualization, Funding acquisition, Writing - review & editing. **Chunya Li:** Conceptualization, Supervision, Writing - review & editing. **Nianjun Yang:** Writing - review & editing.Acknowledgements

The authors gratefully acknowledge the financial supports from The National Natural Science Foundation of China, China (No. 21874157,21675175 and 21275166), Major Projects of Technical Innovation of Hubei Province, China (No. 2017ACA172), Natural Science Foundation of Hubei Province, China (No. 2018CFB617 and 2015CFA092), and the Fundamental Research Funds for the Central Universities",South-Central University of Nationalities, China (CZY18031).

Conflict of interest

The authors declare no conflict of interest.

Appendix A. Supplementary data

Supplementary data to this article can be found online at https://doi.org/10.1016/j.bios.2019.111540.

References

Cao, S.S., Chen, J.R., Hu, J., 2009. Aust. J. Chem. 62, 1561–1576.
Charakora, C., Thadanipon, K., Chaijindaratana, S., Rattanasiri, S., Numthavaj, P., Thakkinstian, A., 2018. Gynecol. Oncol. 150, 190–200.
Erickson, J.A., Lu, J., Smith, J.J., Bornhorst, J.A., Grenache, D.G., Ashwood, E.R., 2010. Clin. Chem. 56, 1496–1499.
Golub, E., Pelossof, G., Freeman, R., Zhang, H., Willner, I., 2009. Anal. Chem. 81, 9291–9298.
Hagfeldt, A., Boschloo, G., Sun, L.C., Kloo, L., Pettersson, H., 2010. Chem. Rev. 110, 6595–6663.
Huang, Y.B., Liang, J., Wang, X.S., Cao, R., 2017. Chem. Soc. Rev. 46, 126–157.
Ibrahim, I., Lim, H.N., Zawawi, R.M., Tajudin, A.A., Ng, Y.H., Guo, H., Huang, N.M., 2018. J. Mater. Chem. B 6, 4551–4568.
Jia, H.Y., Gao, P.C., Ma, H.M., Li, Y.Y., Gao, J., Du, B., Wei, Q., 2015. Talanta 132, 803–808.
Jiang, H.L., Xu, Q., 2011. Chem. Commun. 47, 3351–3370.
Jiang, H.L., Akita, T., Ishida, T., Haruta, M., Xu, Q., 2011. J. Am. Chem. Soc. 133, 1304–1306.
Kato, H., Torigoe, T., 1977. Cancer 40, 1621–1628.
Li, X.J., Zhang, X.Y., Ma, H.M., Wu, D., Zhang, Y., Du, B., Wei, Q., 2014a. Biosens. Bioelectron. 55, 330–336.
Li, S.H., Luo, J.H., Yang, X.F., Wan, Y., Liu, C.H., 2014b. Sens. Actuators B Chem. 197, 43–49.
Li, Y.Y., Zhang, Y.H., Li, F.Y., Feng, J.H., Li, M.D., Chen, L., Dong, Y.H., 2017a. Biosens. Bioelectron. 92, 33–39.
Li, M.S., Wang, Y.Y., Ye, X.X., Wang, Z.G., Wu, T.H., Li, C.Y., 2017b. Microchim. Acta 184, 3565–3572.
Li, L., Zheng, X.X., Huang, Y.Z., Zhang, L.N., Cui, K., Zhang, Y., Yu, J.H., 2018. Anal.

Chem. 90, 13882–13890.
Liu, Y.L., Tang, Z.Y., 2013. Adv. Mater. 25, 5819–5825.
Liu, Y.Y., Ma, H.M., Gao, J., Wu, D., Ren, X., Yan, T., Pang, X.H., Wei, Q., 2016. Biosens. Bioelectron. 79, 71–78.
Luo, Z.B., Zhang, L.J., Zeng, R.J., Su, L.S., Tang, D.P., 2018. Anal. Chem. 90, 9568–9575.
Rodenas, T., Luz, I., Prieto, G., Seoane, B., Miro, H., Corma, A., Kapteijn, F., Llabrés i Xamena, F.X., Gascon, J., 2015. Nat. Mater. 14, 48–55.
Silva, P., Vilela, S.M., Tomé, J.P., Almeida Paz, F.A., 2015. Chem. Soc. Rev. 44, 6774–6803.
Sturgeon, C.M., Duffy, M.J., Hofmann, B.R., Lamerz, R., Fritsche, H.A., Gaarenstroom, K., Bonfrer, J., Ecke, T.H., Grossman, H.B., Hayes, P., Hoffmann, R.T., Lerner, S.P., Löhe Louhimo, F.,J., Sawczuk, I., Taketa, K., Diamandis, E.P., 2010. Clin. Chem. 56, e1–48.
Tada, H., Fujishima, M., Kobayashi, H., 2011. Chem. Soc. Rev. 40, 4232–4243.
Tan, Y., Wang, Y.Y., Li, M.S., Ye, X.X., Wu, T.H., Li, C.Y., 2017. Biosens. Bioelectron. 91, 741–746.
Tan, Y., Li, M.S., Ye, X.X., Wang, Z.G., Wang, Y.Y., Li, C.Y., 2018. Sens. Actuators B Chem. 262, 982–990.
Tian, P.L., Shen, K., Chen, J.Y., Fan, T., Fang, R.Q., Li, Y.W., 2018. Small Meth 2, 1800219.
Wang, B., Lv, X.L., Feng, D., Xie Zhang, L.H., Li, J.,M., Zhou, H.C., 2016. J. Am. Chem. Soc. 138, 6204–6216.
Wu, D., Fan, H.X., Li, Y.Y., Zhang, Y., Liang, H.X., Wei, Q., 2013. Biosens. Bioelectron. 46, 91–96.
Wu, D., Guo, A.P., Guo, Z.K., Xie, L.L., Wei, Q., Du, B., 2014. Biosens. Bioelectron. 54, 634–639.
Wu, Y.Y., Zhao, Y., Wang, Y.Y., Ye, X.X., Wu, T.H., Deng, H.P., Wu, P., Li, C.Y., 2017. Biosens. Bioelectron. 96, 140–145.
Xia, W., Mahmood, A., Zou, R.Q., Xu, Q., 2015. Energy Environ. Sci. 8, 1837–1866.
Xu, R., Wei, D., Du, B., Cao, W., Fan, D.W., Zhang, Y., Wei, Q., Ju, H.X., 2018. Biosens. Bioelectron. 122, 37–42.
Yang, R.Y., Zou, K., Li, Y.M., Meng, L.X., Zhang, X.H., Chen, J.H., 2018. Anal. Chem. 90, 9480–9486.
Ye, X.X., Li, M.S., Hu, Y., Wang, Z.G., Wang, Y.Y., Deng, H.P., Xiong, X.X., Li, C.Y., Sun, D., 2018. Sens. Actuators B Chem. 275, 199–205.
Yu, X.Y., Wang, Y.Y., Chen, X.M., Wu, K.B., Chen, D.C., Ma, M., Huang, Z.J., Wu, W.Z., Li, C.Y., 2015. Anal. Chem. 87, 4237–4244.
Zhang, X.Y., Li, F., Wei, Q., Du, B., Wu, D., He, H., 2014. Sens. Actuators B Chem. 194, 64–70.
Zhang, Y.F., Wang, M.D., Wang, Y.G., Feng, J.H., Zhang, Y., Sun, X., Du, B., Wei, Q., 2019. Biosens. Bioelectron. 126, 23–29.
Zhao, Q.Y., Duan, R.Q., Yuan, J.L., Quan, Y., Yang, H., Xi, M.R., 2014. Int. J. Nanomed. 9, 1097–1104.
Zhao, W., Yu, H.X., Han, Z.F., Gao, N., Xue, J.R., Wang, Y., 2015. Int. J. Clin. Exp. Pathol. 8, 9506–9511.
Zhao, M.T., Lu, Q.P., Ma, Q.L., Zhang, H., 2017. Small Meth 1, 1600030.
Zhou, H.C., Kitagawa, S., 2014. Chem. Soc. Rev. 43, 5415–5418.
Zhou, X., Wang, Y.Y., Li, C.Y., Wu, T.H., 2019. Chem. Eng. J. 372, 46–52.